

Spectral clustering applied for dynamic contrast-enhanced MR analysis of time–intensity curves

Guillaume Tartare^{a,b}, Denis Hamad^b, Mustapha Azahaf^{a,b,c}, Philippe Puech^{a,b,c}, Nacim Betrouni^{a,b,*}

^a INSERM, U703, 152 rue du Docteur Yersin, 59120 CHRU Lille, France

^b Université Littoral Côte d'Opale, Laboratoire d'Informatique, Signal et Image de la Côte d'Opale, France

^c Service de Radiologie, Hôpital Claude Huriez, CHRU de Lille, France

ARTICLE INFO

Article history:

Received 12 February 2014

Received in revised form 24 June 2014

Accepted 21 July 2014

Keywords:

Curves analysis

Dynamic contrast-enhanced

(DCE)–magnetic resonance imaging (MRI)

Non-parametric analysis

Spectral clustering

ABSTRACT

Dynamic contrast-enhanced (DCE)–magnetic resonance imaging (MRI) represents an emerging method for the prediction of biomarker responses in cancer. However, DCE images remain difficult to analyze and interpret. Although pharmacokinetic approaches, which involve multi-step processes, can provide a general framework for the interpretation of these data, they are still too complex for robust and accurate implementation. Therefore, statistical data analysis techniques were recently suggested as another valid interpretation strategy for DCE–MRI.

In this context, we propose a spectral clustering approach for the analysis of DCE–MRI time–intensity signals. This graph theory-based method allows for the grouping of signals after spatial transformation. Subsequently, these data clusters can be labeled following comparison to arterial signals. Here, we have performed experiments with simulated (i.e., generated via pharmacokinetic modeling) and clinical (i.e., obtained from patients scanned during prostate cancer diagnosis) data sets in order to demonstrate the feasibility and applicability of this kind of unsupervised and non-parametric approach.

© 2014 Elsevier Ltd. All rights reserved.

1. Introduction

Magnetic resonance imaging (MRI) has become a reference technique for the diagnosis and staging of several types of cancer, including prostate, breast, and liver tumors. The typical multiparametric MRI protocol involves morphologic acquisition of T1-weighted (T1W) and/or T2-weighted (T2W) images as well as functional imaging using diffusion, spectroscopy, and perfusion sequences. Indeed, perfusion or dynamic contrast enhanced (DCE) imaging, which is acquired following injection of a contrast agent, is commonly employed to enhance the characterization of early cancers prior to therapy and to monitor their progression during and after anti-angiogenic or mini invasive treatments [1]. Angiogenesis appears to play a central role in the growth and spread of tumors [2,3]. When a tumor grows, the capillary network proliferates due to the release of pro-angiogenic factors, and the permeability of capillary walls increases [4]. Also, it is known that DCE–MRI can

allow the visualization of these aberrant microcirculation modifications, which represent a valid biomarker for cancer development [5,6].

DCE–MRI involves rapid and repeated acquisition of T1W images before, during, and after the injection of a low molecular weight paramagnetic contrast agent. There are three ways to analyze these time-dependent signal-intensity curves: qualitative, semi-quantitative, and quantitative.

Qualitative evaluation uses simple visual assessment, such as Kuhl's technique [7], whereas semi-quantitative analysis provides a set of parameters based on contrast agent dynamics (i.e., wash in [uptake], peak, and wash out [loss over time]) [8]. Although, the semi-quantitative method is reproducible, it can be heavily influenced by the selected protocol [9]. Moreover, it is not useful for precisely determining changes in contrast agent concentration, and therefore does not directly yield data on tissue physiology.

In contrast to the two previous approaches, quantitative analysis is based on a pharmacokinetic model. The model conceptualizes the exchange of a low-molecular weight contrast medium between the intravascular and the extravascular extracellular spaces (EES) in the tissue. The application of this model to DCE–MRI data makes it possible to establish physiologic parameters, such as vessel permeability, perfusion, blood volume, K_{trans} (transfer constant between

* Corresponding author at: INSERM, U703 152, rue du Docteur Yersin, Lille University Hospital (CHRU de Lille), 59120 Loos, France. Tel.: +33 3 20 44 67 22.

E-mail addresses: nacim.betrouni@inserm.fr, n-betrouni@chru-lille.fr (N. Betrouni).

blood plasma and EES), K_{ep} (exchange constant rate between EES and blood plasma), and V_e (extravascular extracellular volume) [10]. It should be noted that clinical implementation of this technique in routine imaging protocols has remained limited. This is due to the fact until 2012, there was no standardized and generally accepted protocols for DCE–MRI. In 2012, the Quantitative Imaging Biomarkers Alliance (QIBA) DCE–MRI Technical Committee from the Radiological Society of North America (RSNA) published recommendations to define basic standards for DCE–MRI measurements and quality control with the goal of promoting consistent and reliable results across platforms, clinical sites, and time [11]. According to these recommendations, QIBA DCE–MRI committee suggested the use of Toft's model as pharmacokinetic model.

However, quantitative signal analysis is a complex, multi-step process. In fact, several studies focusing on this technique have demonstrated the difficulty of reproducing and repeating these physiological parameter measurements [9,12]. Quantitative analysis involves T1 mapping, transformation of signal intensity time curves $S(t)$ into contrast agent concentration time curves $C(t)$, and arterial input function measurement (AIF). Moreover, several techniques and approaches can be applied to achieve each of these steps. To further complicate matters, there remains a lack of consensus regarding standardized cutoff values for K_{trans} , K_{ep} , and V_e for clinical applications.

To overcome the limitations of the methods in the literature, data analysis techniques were investigated for interpreting quantitative information [15] (Cluster analysis of the signal curves in perfusion DCE–MRI datasets). In fact, promising results were obtained without any prior knowledge of the underlying tissue vasculature and arterial input function. Indeed, no assumptions about the data distribution, pharmacokinetic model, or AIF model could be established. In these approaches, the aim was to group the voxels into homogeneous patterns that share the same properties. Each voxel is represented by a time–intensity curve, which is obtained by converting each frame of sequential images into a one-dimensional row signal vector. Each curve can then be characterized based on three states: wash in, peak, and wash out. Although these curves display similar shapes, their evolutions and magnitudes are tissue dependent. Fig. 1 depicts typical signatures for characterizing tissue health status (e.g., tumor, healthy, and suspicious tissues).

In addition, independent components analysis (ICA) has been used in recent studies [13,14]. In fact, Wu and Liu [13] applied ICA to the assessment of cerebral blood perfusion, analyzing the data as a summation of brain hemodynamic behaviors and external perturbations (head movements, physiological pulsations, and machine noise). Therefore, by assuming the spatial independence of the hemodynamic patterns and artificial processes, the ICA could be used to separate mixed signals and reveal brain hemodynamic abnormalities. On the other hand, Mehrabian et al. [14] developed an adaptive, complex ICA technique to distinguish extravascular and extracellular signals. This method was employed to calculate intravascular time–intensity curves, allowing separation of these signals during DCE–MRI of tumors.

Furthermore, Chen et al. [15] introduced a probabilistic based approach where compartmental analysis was combined with convex analysis in order to determine pixel-wise partial volume effects, which can result in mixing of more than one compartment. Notably, this method is parametric and assumes Gaussian distribution of signal curves. More recently, Agner et al. [16] introduced a spectral embedded active contour technique. They employed this spectral-based approach to perform non-linear dimensionality reduction to drive an active contour, which could be used to segment breast lesions on DCE–MRI. Notably, this study reported the first results concerning the applicability of spectral techniques for reducing image space in DCE.

In the present study, we investigated the use of a graph-based approach (i.e., spectral clustering) to analyze DCE–MRI time–intensity signals. In contrast to parametric methods, graph-based methods are non-parametric and do not require a priori assumptions about the size, shape, or distribution of clusters [17]. Our global approach was comprised of two steps: clustering and interpretation. The clustering step involved space embedding of the curves to make them linearly separable, and results were grouped based on homogenous patterns. On the other hand, the interpretation step was used to classify patterns according to their distance from the artery, with results presented as distance maps. This interpretation strategy is justified based on the assumption that tumor angiogenesis represents a principal factor that determines tumor growth and spread as well as increased capillary permeability. We propose that the map resulting from our approach

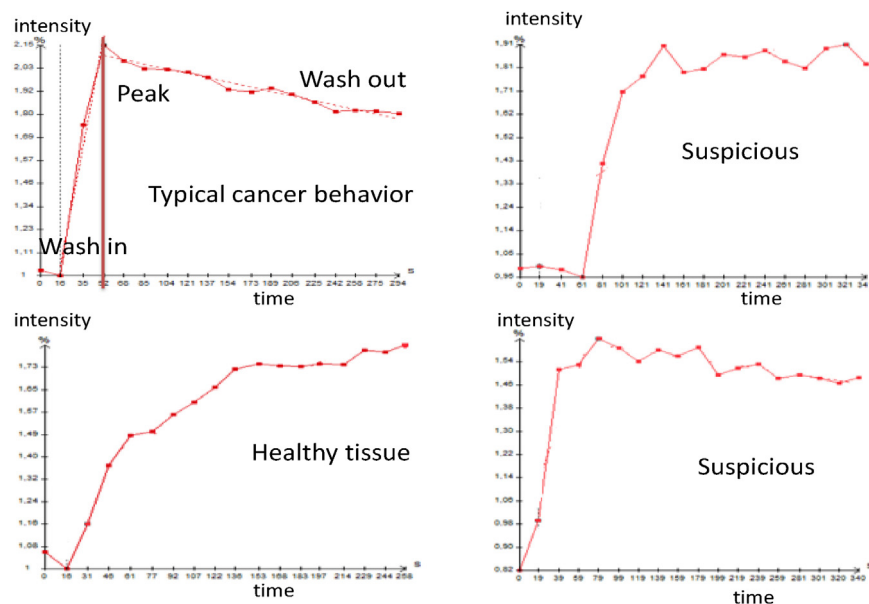


Fig. 1. Time–intensity curves extracted from DCE magnetic resonance images for four cases. Typical behavior of tumor (top-left), healthy (bottom-left), and suspicious (top-right and bottom-right) tissues. Note the shape difference of the last two curves.

could be combined with data obtained from other quantitative or qualitative methods in order to enhance DCE–MRI interpretation.

In the following sections, we provide a background on graph-based clustering as well as a description of theoretical aspects associated with spectral clustering. In addition, we describe the application of this technique to the analysis of DCE–MRI (Section 3), which was illustrated using experimental systems based on synthetic and clinical data (Section 4). Finally, we discuss the spectral clustering method along with our results and provide conclusions for our study (Section 5).

2. Background

Graph-based clustering involves constructing a weighted graph in which the data points within each vertex are associated with a point, and the similarity between two points is determined by a weighted edge connecting the two vertices [18–20].

2.1. Spectral clustering approach

Let us consider a set of data points where $X = \{x_1, \dots, x_i, \dots, x_n\}$, with each $x_i = (x_{i1}, \dots, x_{it}, \dots, x_{im})^T$. We define an affinity graph $G = (V, E, W)$ as an undirected graph where the i th vertex in V corresponds to the point x_i , and each edge $(i, j) \in E$ is associated with a weight w_{ij} , which denotes the similarity (or affinity) of the points x_i and x_j . Moreover, the similarity matrix $W \in R^{n \times n}$ is represented by the term w_{ij} , which can be of cosine, fuzzy, or Gaussian type. However, a Gaussian function (Eq. (1)) is often used in spectral clustering approaches:

$$w_{ij} = \exp\left(-\frac{1}{2\sigma^2}d^2(x_i, x_j)\right) \quad (1)$$

Here, the scaling parameter σ of the Gaussian function (1) is used in the similarity matrix to control how rapidly the similarity w_{ij} falls off in relation to the Euclidean distance, $d(x_i, x_j)$, between points x_i and x_j . Thus, the use of a Gaussian kernel instead of a linear model aims to accentuate the local influence.

There are various ways to construct a graph that represents the relationships between dataset x .

- Fully connected graphs: all vertices that have non-null similarities are connected with each other.
- ε -neighborhood graphs: each vertex is connected to vertices that fall inside a hyper-sphere of radius ε , where ε is a real value that must be tuned in order to contain the local data structure.
- k -nearest neighbor graphs: each vertex is connected to its k -nearest neighbors where k is an integer number that controls the local relationships between data.

Notably, k -nearest neighbor and ε -neighborhood graphs are the most suited for clustering problems [20].

The overall goal of spectral clustering is to partition the data into K clusters (groups), such that each x_i belongs to only one cluster. Thus, $\{V_1, \dots, V_k\}$ denotes a partition of V , and for two subsets of V (V_1 and V_2), the similarity is defined by the objective cut function:

$$C(V_1, V_2) = \sum_{i \in V_1} \sum_{j \in V_2} w_{ij} \quad (2)$$

This equation represents the sum of weight connections between V_1 and V_2 .

Spectral clustering is typically used in its normalized form [19] by optimizing the following objective function:

$$J_{\text{ncut}} = \sum_{i=1}^k \frac{C(V_i, V) - C(V_i, V_i)}{C(V_i, V)} \quad (3)$$

The numerator in the i th term is equal to the sum of the similarities leaving of the subset V_i and the denominator is equal to the total degree of the subset V_i . Minimizing the sum of these terms results in partitioning so that edges with large similarities tend to stay within the individual subsets V_i and that the volumes of V_i are balanced.

In its discrete form, the optimization problem is intractable when rewriting Eq. (3) in its normalized quadratic form, which involves indicator vectors. Also, spectral clustering applies a standard relaxation procedure, in which indicator vectors are replaced with real-valued vectors. This produces a generalized eigenproblem, which can be summarized conveniently in terms of the normalized graph Laplacian of W defined as follows:

$$L = D^{-1/2}(D - W)D^{-1/2} = I - D^{-1/2}WD^{-1/2} \quad (4)$$

In this equation, $D = \text{diag}(d_1, \dots, d_n)$ is the degree matrix, with $d_i = \sum_{j=1}^n w_{ij}$, $i = 1, \dots, n$ representing the degree of the i th vertex.

2.2. Spectral clustering algorithm

Spectral clustering algorithms typically consist of the following three basic steps [21]:

1. Pre-processing Construct the graph and the similarity matrix to represent the dataset.
2. Spectral embedding
 - Form the associated Laplacian matrix.
 - Compute eigenvalues and eigenvectors of the Laplacian matrix.
 - Map each point to a lower-dimensional representation based on one or more eigenvectors.
3. Clustering Assign points to two or more classes, based on the new representation.

2.3. Tuning of parameters

The Gaussian kernel is the most common similarity function in the clustering domain, and its free parameter is the kernel radius σ . Notably, this parameter is often examined in standard spectral algorithms, and different σ values can result in vastly different clustering results.

Instead of selecting a single scaling parameter σ , a local scaling parameter σ_i for each data point x_i is calculated as previously described [22], where $\sigma_i = d(x_i, x_{r(i)})$ is the distance between x_i and its r th neighbored $x_{r(i)}$. The selection of the rank r is scale independent and is usually between 7 and 10. Therefore, for each pair of points (x_i, x_j) , the connection weight w_{ij} is given by:

$$w_{ij} = \exp\left(-\frac{1}{2\sigma_i\sigma_j}d^2(x_i, x_j)\right) \quad (5)$$

Indeed, using a specific scaling parameter for each data point allows for self-tuning of the point-to-point distances according to the local statistics of their neighborhoods.

After defining a scheme in order to set the scale parameter automatically, we are left with only one free parameter: the number of clusters.

2.4. Automatic determination of the number of clusters

The principal difficulty in spectral clustering algorithms is the estimation of the number of clusters. The eigengap technique, which is commonly used to estimate this number, is performed by searching for a drop in the magnitude of eigenvalues that are arranged in an increasing order. The goal of this method is to choose the number k of clusters, such that all eigenvalues $\lambda_1, \dots, \lambda_k$ are very

small, but the λ_{k+1} is relatively large. The gap between successive eigenvalues is defined as a difference:

$$\Delta_k = |\lambda_k - \lambda_{k+1}| \quad (6)$$

Thus, the optimal number of clusters is given by:

$$\hat{k} = \arg \max(\Delta_k) \quad (7)$$

However, if the eigengap maximum is relatively small, it becomes hard to precisely estimate the number of clusters. In this regard, White and Smith proposed another approach [23], which employed a previously described graphing concept for identifying communities [24].

Their modularity function J_{mod} can be defined as:

$$J_{\text{mod}} = \sum_{i=1}^k \frac{1}{|V_i|} \left[\frac{C(V_i, V_i)}{C(V, V)} - \left(\frac{C(V_i, V)}{C(V, V)} \right)^2 \right] \quad (8)$$

In this equation, $|V_i|$ is the cardinal of V_i , $C(V_i, V_i)$ for measuring the within-cluster sum of weights, whereas $C(V_i, V)$ measures the sum of weights over all edges attached to vertices in cluster i , and $C(V, V)$ measures the sum of all edges in the graph. Modularity function is computed versus the number of clusters, with the maximum value yielding the estimated number of clusters.

More recently, Yu and Ding [25], showed that Eq. (8) was related to ratio-cut, and they proposed to solve modularity clustering via normalized cut using the following objective function:

$$J_{\text{nmod}} = \sum_{i=1}^k \frac{1}{C(V_i, V)} \left[\frac{C(V_i, V_i)}{C(V, V)} - \left(\frac{C(V_i, V)}{C(V, V)} \right)^2 \right] \quad (9)$$

In the present work, we propose to compute J_{nmod} based on the number of clusters k , with the estimated number of clusters corresponding to the maximum normalized modularity defined in Eq. (9).

3. Materials and methods

A global description of our approach is presented in Fig. 2. It was comprised of two steps: the first step involved clustering in order to classify the voxels into homogeneous classes and the second step

introduced additional knowledge for cluster interpretation through comparison to reference signals extracted from the artery.

Time-intensity curves $\{x_1, \dots, x_i, \dots, x_n\}$ were obtained by converting each voxel of each frame (from the sequential images) into a 1D row, denoted by $x_i = (x_{i1}, \dots, x_{it}, \dots, x_{im})^T$, where n is the total number of voxels and m represents the number of temporal scans (i.e., number of acquisitions). Notably, the curve signals were used as inputs for the clustering algorithm. In this context, a graph was constructed, in which each curve was associated with a vertex, and the edge weights between vertices were a function of the distance between their related curves. The data signal structure could then be defined by this graph and its associated Laplacian matrix.

3.1. Implementation of the spectral clustering algorithm

A region of interest (ROI), surrounding the tissue to be analyzed, was selected by experts with knowledge of anatomy. In clinical practice, the quantitative analysis of these images was most often performed following a preliminary visual analysis in order to detect regions with contrast agent uptake.

3.1.1. Pre-processing

Three processing steps were applied to the ROI.

The signal presented three characteristics that could interfere with the classification process: delayed bolus arrival, intensity, and noise. In order to properly record bolus arrival in the body, MRI acquisition was started prior to contrast agent injection. Notably, images acquired before injection could not provide information on tissue perfusion. Also, it was necessary to detect the peak time of contrast agent arrival to the study area because images needed to be acquired before this peak was achieved. Peak time could automatically be determined following artery detection. This step is detailed in Section 3.2.1.

The second pre-processing step aimed to reduce any amplitude effect. For this, normalization was applied as:

$$x_{it} = \frac{x_{it} - \min(x_i)}{\max(x_i) - \min(x_i)} \quad (10)$$

The final pre-processing step involved filtering, where a sliding window of size 3 was applied to the wash out part of the curve.

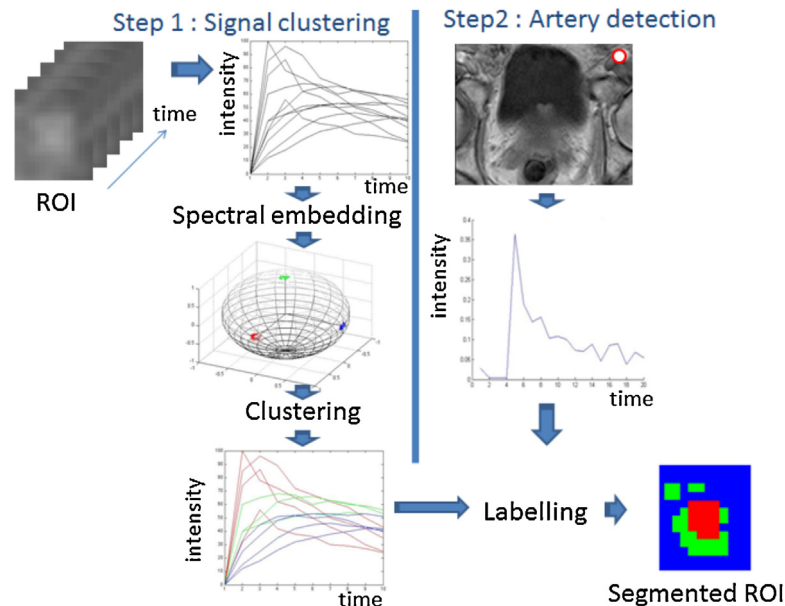


Fig. 2. The DCE-MRI analysis method. Arrows indicate the processing steps. The clustering step (left) is performed once the curves are extracted and space transformation is completed. Artery detection (right) is achieved by labeling the results from the first step.

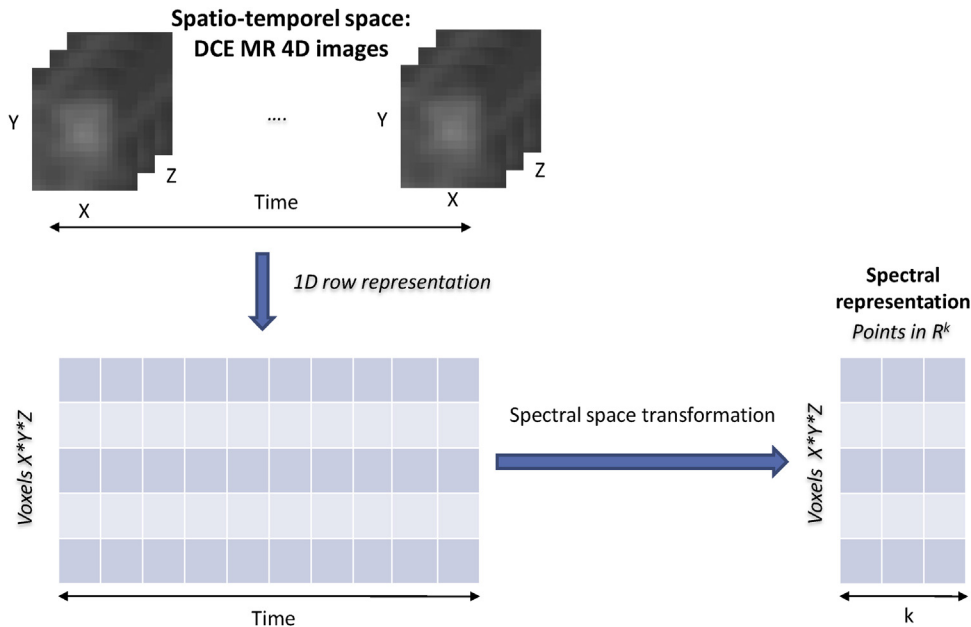


Fig. 3. From data representation to spectral representation: space reduction.

The goal of this step was to reduce noise without distorting peak position and magnitude.

3.1.2. Similarity matrix construction

The similarity matrix (W) was constructed based on the concept that each element w_{ij} represented the similarity between each pair of curves x_i and x_j . Thus, Eq. (1) of the previous section becomes:

$$w_{ij} = \exp \left(-\frac{1}{2\sigma_i\sigma_j} \sum_{t=1}^m (x_{it} - x_{jt})^2 \right) \quad (11)$$

In this equation, m is the number of temporal scans.

The choice of the techniques is justified by the fact that the analysis technique deals with the curves shapes rather than the absolute signals and its important to take into consideration the underlying physiological phenomenon. Moreover, this kind of techniques proved to be very efficient to deal with temporal signals ([15,26]). In a comparative study by Kruggel et al. [27] different smoothing techniques were tested and evaluated on temporal signals from functional MRI. One of the conclusions is that moving average filter exhibits competitive results.

3.1.3. Spectral representation

The spectral representation was obtained by associating the eigenvectors of the Laplacian graph with the similarity matrix. Only the k top eigenvalues were kept, with k being the number of classes estimated in the next section (Fig. 3).

3.1.4. Automatic estimation of the number of clusters

Estimation of the number of clusters was achieved using the normalized modularity criterion, J_{nmod} (Eq. (9)). The algorithm was iterated by varying the class numbers starting from two. For each iteration, the modularity criterion was computed, with its maximum defining the number of classes. Fig. 4 shows an example where the optimal number of classes is three.

3.1.5. Clustering step

As a result of spectral transformation (Fig. 3), the projected data could be easily separated using a simple algorithm like k -means. However, in order to overcome any initialization weakness

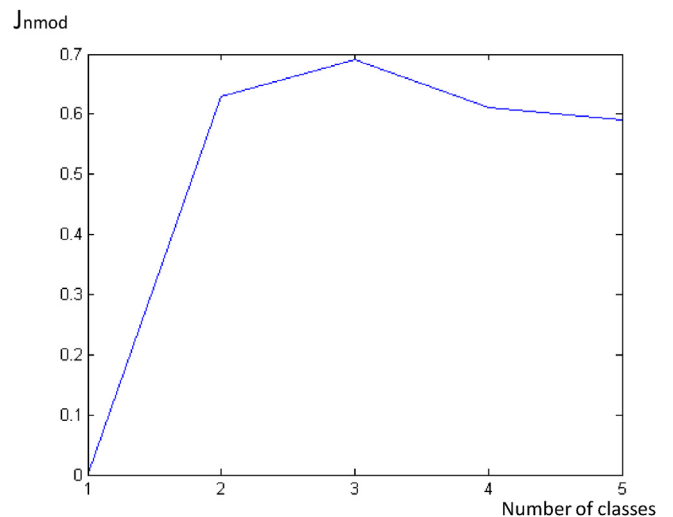


Fig. 4. Curve representing the value of J_{nmod} as a function of the number of classes. The maximum of this curve indicates the optimal number of classes.

of k -means, we randomly generated the initialization 100 times, selecting the best solution according to the mean square error criterion between the centers of the calculated classes and the elements contained in those classes. At the end of this procedure, the clusters could be used to label the signal curves (Fig. 2), and therefore their corresponding voxels.

3.2. Interpretation of cluster labels

In order to provide a label or interpretation for each cluster, a distance criterion was defined based on quantification of signal behaviors in the cluster using reference behaviors, which were extracted from the artery. This interpretation strategy was justified by the assumption that angiogenesis is one of the factors contributing to the growth and spread of tumors, inducing increased permeability of capillary walls. For this purpose, the artery needs to be detected.

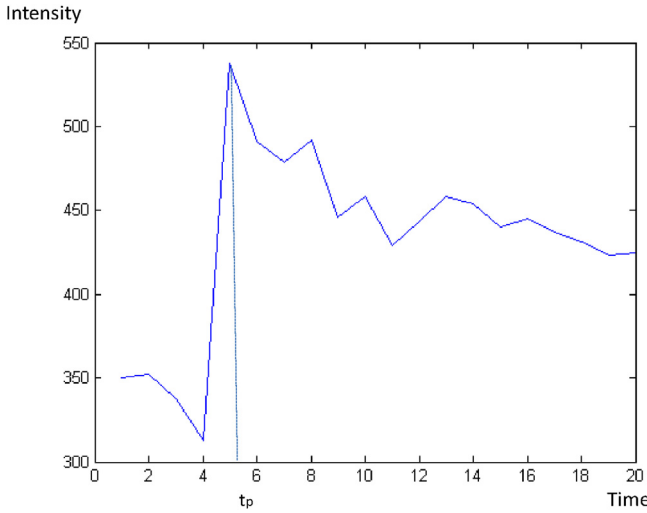


Fig. 5. Time-intensity curve of a voxel located on an external iliac artery for the prostate.

3.2.1. Arterial detection

Utilizing an approach proposed by Chen et al. [28], we have developed an arterial detection strategy. The temporal signal of an artery can be characterized by high amplitude at time to peak (t_p), a steep slope, and a spatially cylindrical shape (Fig. 5). Therefore, our method involved four filters to adjust certain parameters, including threshold, contrast detection, and spatial aspects.

Indeed, arteries display a large amount of contrast agent flowing through them, which can cause the image voxels of arteries to brighten more than most other voxels. For this reason, the peak height of an artery is typically higher than most others. Thus, we first implemented a thresholding filter following Eq. (12). It allowed for the removal of voxels with small peak curves.

$$x(t_p) < \mu \quad (12)$$

Here, $x(t)$ signifies the time-intensity values, t_p is the time to peak, and μ represents the mean peak values of all voxels in the image corresponding to the t_p position.

The second filter was employed to detect fast contrast during wash in of contrast agent in artery voxels. For this, the signal enhancement ratio at each time point was computed using Eq. (13):

$$R(t) = \frac{x(t)}{x_0} \quad (13)$$

$R(t)$ represents the ratio of signal enhancement from baseline to time t and x_0 is the baseline signal, which was computed as the average signal of the time points during the wash in. The slope was defined by Eq. (14):

$$\text{slope} = \frac{R(t_p) - 1}{t_p} \quad (14)$$

Only the top 20% greatest slopes were retained as arterial candidates.

The two previous filters dealt with temporal aspects of the artery, whereas the two remaining filters pertain to spatial qualities. A region labeling process was applied in order to form distinguishable 2D connected components based on the candidate voxels from each axial slice. Also, a size filter was utilized to retain only those patterns with sufficient voxels to be part of an artery. For each voxel's pattern, the average peak time was calculated, and only those patterns with the lowest 20% of time to peak were kept.

The following step was used to calculate the circularity C_z of each remaining region following Eq. (15):

$$C_z = \frac{A}{P^2} \quad (15)$$

Here, P represents the perimeter. It is computed by calculating the distance between each adjoining pair of voxels around the border of the region. A , the area, is the actual number of voxel in the region.

The 2D patterns were propagated in a transverse direction to form 3D patterns. For this process, 2D patterns that overlapped in the axial slices (above or below) were considered to belong to the same 3D object. The cylindricity of each 3D pattern was then calculated by summing (across the axial slices) the circularity of each 2D pattern forming the same 3D object as in Eq. (16):

$$C_y = \sum_z C_z \quad (16)$$

C_y is the cylindricity of the object. The most cylindrical object was considered to be the artery.

Once the artery was detected, the last step involved estimating its median signal. To this end, for each 2D cluster, a median value was computed from the pixels. The 2D median values were stored together to form the reference signal curve denoted as x_a .

3.2.2. Labeling of clusters

To establish the labeling of clusters, a comparison was made by computing the distance d_{ja} between the signal of the artery x_a and the median signal \hat{x}_j used as prototype of cluster (j):

$$d_{ja}^2 = \sum_{t=1}^m (x_{at} - \hat{x}_{jt})^2 \quad (17)$$

The aim of this comparison was to order the clusters according to their distances from the detected artery. This is important because it can relate valuable information about the nature of the tissue.

Ideally, this clustering procedure could be used to assign ROI voxels into clusters that are indicative of the tissue vascularization according to their behaviors. However, MRI is noisy and can lead to an overestimation of the number of clusters. Thus, to reduce this overestimation, our clusters were ordered according to the distance between their prototypes and reference artery signals. They were grouped together when the distance between them was less than a defined threshold. Experimentally, we found that the optimal merging threshold was 10% of the highest distance value between prototypes. Notably, this merging decision made interpretation easier.

4. Experiments and results

Here, we report the results obtained after applying our method to either synthetic data (based on pharmacokinetic models with known ground truths of tumor distributions) or clinical images (correlated with histopathology findings).

4.1. Synthetic data

4.1.1. Data generation

Validated pharmacokinetic models were used to generate simulations. A large set of synthetic DCE-MRI time series were constructed without assumptions regarding data distribution. However, the generated data contained some aspects of real situations, including the following: (i) the bolus did not appear immediately, (ii) different curve behaviors occurred, and (iii) various organ scenarios were possible.

Curves were based on the work of Chen et al. [15], with additional behavioral possibilities. All curves were displayed as

Table 1

Quantitative results from spectral clustering analysis of 7 simulated cases examined by dynamic contrast-enhanced-magnetic resonance imaging.

	Case 1	Case 2	Case 3	Case 4	Case 5	Case 6	Case 7
Number of simulated cancers	3	2	1	3	3	1	0
Number of detected cancers	3	2	1	3	3	1	0
Sensitivity (or recall)	1.00	0.97	1.00	0.96	0.97	1.00	–
Specificity	0.99	1.000	0.86	1.00	1.00	1.00	0.84
Precision	0.99	0.99	0.61	0.99	0.99	1.00	0.50
F-measure	0.99	0.98	0.76	0.98	0.98	1.00	–
True Positive (voxels)	243	92	25	92	73	218	0
False Positive (voxels)	1	0	83	0	0	0	40
False Negative (voxels)	0	2	0	3	2	0	0
True Negative (voxels)	506	634	513	455	408	666	220

concentration of contrast agent over time. These 1D simulations were then combined with a 3D model of the prostate: Prostate Atlas [29] to obtain 4D data set. The data were immersed in an environment containing the iliac and the obturator artery.

For each voxel, the evolution of the concentration was modeled using Eq. (18):

$$C_j(t) = k_{j,trans} C_p(t) \otimes \exp(-k_{ep,j}t) \quad (18)$$

In this equation, \otimes denotes the mathematical convolution operation.

In addition, the plasmatic concentration, $C_p(t)$, was generated using the Weinman model:

$$C_p(t) = D(a_1 e^{-m_1 t} + a_2 e^{-m_2 t}) \quad (19)$$

D is the contrast agent dose (0.1 mM/Kg). Two arterial input function parameters (a_1 , a_2 , m_1 , and m_2) were considered: those proposed by Weinmann et al. [30] ($a_1 = 3.99$, $a_2 = 4.78$, $m_1 = 0.144$ et $m_2 = 0.011$ and those used by Chen et al. [15] ($a_1 = 3.99$, $a_2 = 0.78$, $m_1 = 1$ et $m_2 = 0.011$).

In order to achieve different behavioral schemes, depending on the tissue nature, distinct pharmacokinetic parameters were chosen (K_{trans} and K_{ep}). For prostate imaging, the following values were reported in the literature [31,32]: $K_{trans} = 0.05 \text{ min}^{-1}$ or 0.2 min^{-1} and $K_{ep} = 0.1 \text{ min}^{-1}$ or 0.4 min^{-1} for healthy prostate tissue, whereas $K_{trans} = 0.4 \text{ min}^{-1}$ or 1 min^{-1} and $K_{ep} = 1.4 \text{ min}^{-1}$ or 2 min^{-1} for prostate lesions.

The generated signals were subsequently perturbed by adding Gaussian noise ($\sigma^2 = 0.2$) in order to obtain more realistic situations. The obtained curves represented the time concentration evolution for each voxel, while in real DCE-MRI data, signals denote time intensity variations. Therefore, the following conversion was realized:

$$x_j(t) = m(t) \sin(\alpha) \frac{1 - e^{-((TR/T_{10}) + C_{pj}(t)TR)}}{1 - \cos(\alpha)e^{-((TR/T_{10}) + R_1 C_{pj}(t)TR)}} \quad (20)$$

with

$$m(t) = m(0)e^{-R_2 C_{pj}(t)TR} \quad (21)$$

In this equation, $m(0)$ equals 6000, α represents the flip angle (17°), TR is the repetition time (8.9 ms), and TE stands for the echo time (4.2 ms). R_1 ($4.5 \text{ s}^{-1} \text{ mM}^{-1}$) and R_2 ($5.5 \text{ s}^{-1} \text{ mM}^{-1}$) are the longitudinal and transverse tissue contrast agent relaxivities. T_{10} (1000 ms) and T_{20}^* are the longitudinal and transverse relaxation times, respectively.

Overall, six cases were generated by varying the number of lesions and their positions on the images (Table 1). A seventh case, representing healthy tissue, was also considered.

4.1.2. Results

Both qualitative and quantitative criteria were used. Qualitative criteria allowed for global appreciation of the method behavior,

whereas quantitative criteria were used to quantify detection. The following quantitative criteria were used:

$$\text{sensitivity} = \frac{\text{True Positive}}{\text{True Positive} + \text{False Positive}} = \text{recall} \quad (22)$$

$$\text{specificity} = \frac{\text{True Negative}}{\text{True Negative} + \text{False Negative}} \quad (23)$$

$$\text{precision} = \frac{\text{True Positive}}{\text{True Positive} + \text{False Positive}} \quad (24)$$

$$F\text{-measure} = 2 \times \frac{\text{precision} \times \text{sensitivity}}{\text{precision} + \text{sensitivity}} \quad (25)$$

Table 1 gives a global description of the synthetic data generated and summarizes our results using the defined criteria.

It clearly appears that the proposed method is efficient: sensitivity (0.96–1.00), specificity (0.86–1.00) and F -measure (0.76–1). These results were mainly due to the non-linear space projection obtained by spectral clustering approach. This fact is highlighted on Fig. 6, which shows these same data clustered by K -means in the input space resulting in lower sensitivity (0.56–0.98), specificity (0.56–1.00) and F -measure (0.00–0.99). Moreover, a comparative study is done with the ICA approach. This later performs better than K -means with sensitivity in (0.91–0.98), specificity in (0.20–1.00) and F -measure in (0.56–1.00). The spectral approach outperforms ICA in all cases except for cases 2 and 4, the ICA sensitivity is slightly better. Globally, sensitivities of both approaches are close while the specificity of our approach is clearly higher.

Fig. 7 depicts the results from four cases, including three tumors with different volumes (case 1), two tumors with distinct volumes (case 2), three tumors that are small but close (case 4), and healthy tissue (case 7).

Fig. 8 highlights the fact that spatial transformation can allow the data to be easily separable using a classification algorithm, such as the K -means.

4.2. Clinical DCE-MRI data studies

We retrospectively analyzed clinical data from seven patients. These individuals were scanned with a multiparametric MRI protocol for prostate cancer diagnosis. Acquisitions were made on a 1.5 T Philips MRI device using an external abdominal coil.

The multispectral MRI data consisted of T2W images with a voxel size of $0.48 \text{ mm} \times 0.48 \text{ mm} \times 2.5 \text{ mm}$ (50 images by volume), T1 DCE with a voxel size of $0.61 \text{ mm} \times 0.61 \text{ mm} \times 4.0 \text{ mm}$ (15 images by volume), 20 acquisitions with a temporal resolution of 15 s, and an apparent diffusion coefficient (ADC) map achieved through diffusion weighting imaging (DWI) ($1.12 \text{ mm} \times 1.12 \text{ mm} \times 4.00 \text{ mm}$ voxel size; 15 images by volume).

Ultimately, all patients underwent radical prostatectomy. Thus, histologic findings can be correlated with the MRI, providing a ground truth for validation of our method. For this purpose, prostate specimens were inked, fixed, and sectioned according to

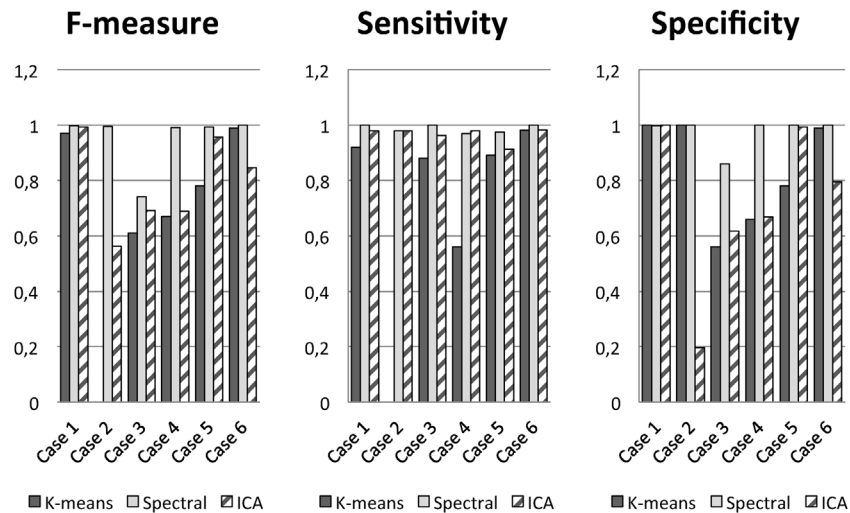


Fig. 6. Comparison of the clustering performances of the proposed approach, the K-means algorithm applied in the input space and ICA approach.

the Stanford protocol [33]. A reconstructed histological map of each prostate was then created. Contours of the histological zones and outlines of each cancer were drawn on the slides while under the microscope. The results from these analyses were reported on MRI via manual correspondence with histology images. Experienced urologists performed this analysis [34]. The prostate was divided into eight regions using the octant technique, with the top and bottom divided into four quadrants: transition zone (TZ), peripheral zone (PZ), left, and right. Within each octant, TZ, PZ, and anterior boundaries of the fibromuscular stroma were traced, and the tumor was located according to these histological points of reference.

Six of the ROI samples were analyzed (from six distinct patients). Five of the specimens were pathological, while the sixth was

extracted from healthy tissue. For each of these clinical samples, starting from the histopathology cards (Fig. 9, column 4), an experienced radiologist defined ROIs containing tumor via DCE-MRI (Fig. 9, columns 1 and 2). For the last patient, the ROI was defined on healthy tissue.

In the five cases involving tumor, the algorithm was able to classify the voxels into three groups (identifying homogeneous classes), which were then sorted according to distance from the artery, indicating regions with differential vascularization (Fig. 9 column 3). The closest corresponded to the tumor. However, the spatial delimitation of this focus was restricted due to fact that hyper-vascularization was present around the tumor area (including the healthy tissue).

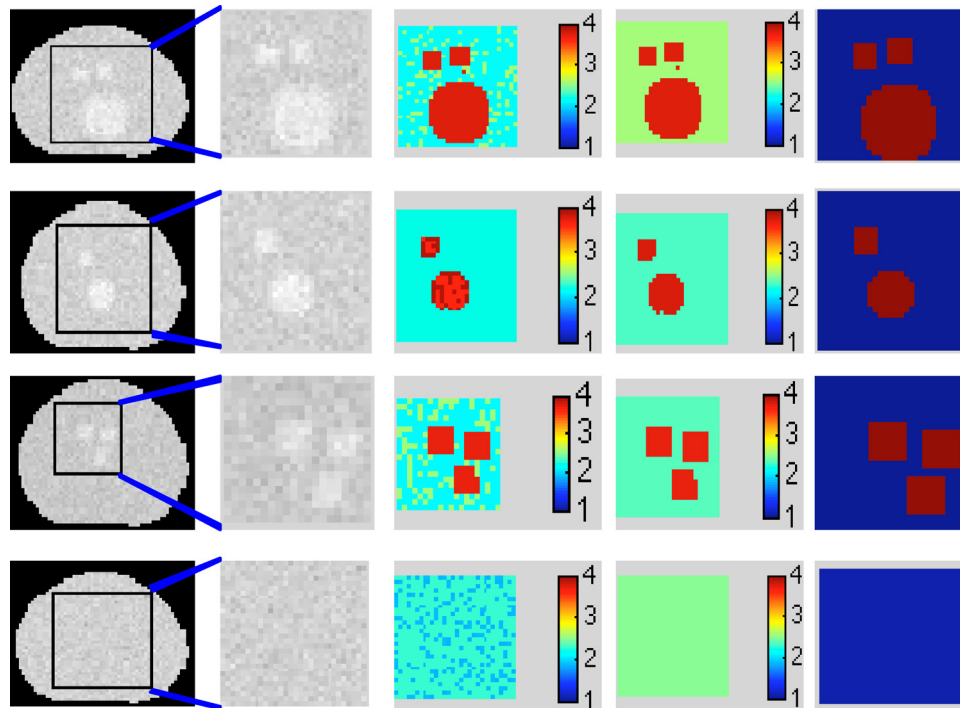


Fig. 7. Results obtained following application of the spectral clustering method to synthetic DCE-MRI on four cases involving different tissue states. Each row illustrates one case. From top to bottom: three tumors with different volumes (case 1), two tumors with distinct volumes (case 2), three tumors that are small but close (case 4), and healthy tissue (case 7). From left to right: synthetic images showing the position of the ROI, zoom of the ROI, clustering results as distance to artery maps, and cluster fusion results. The final column represents the ground truth.

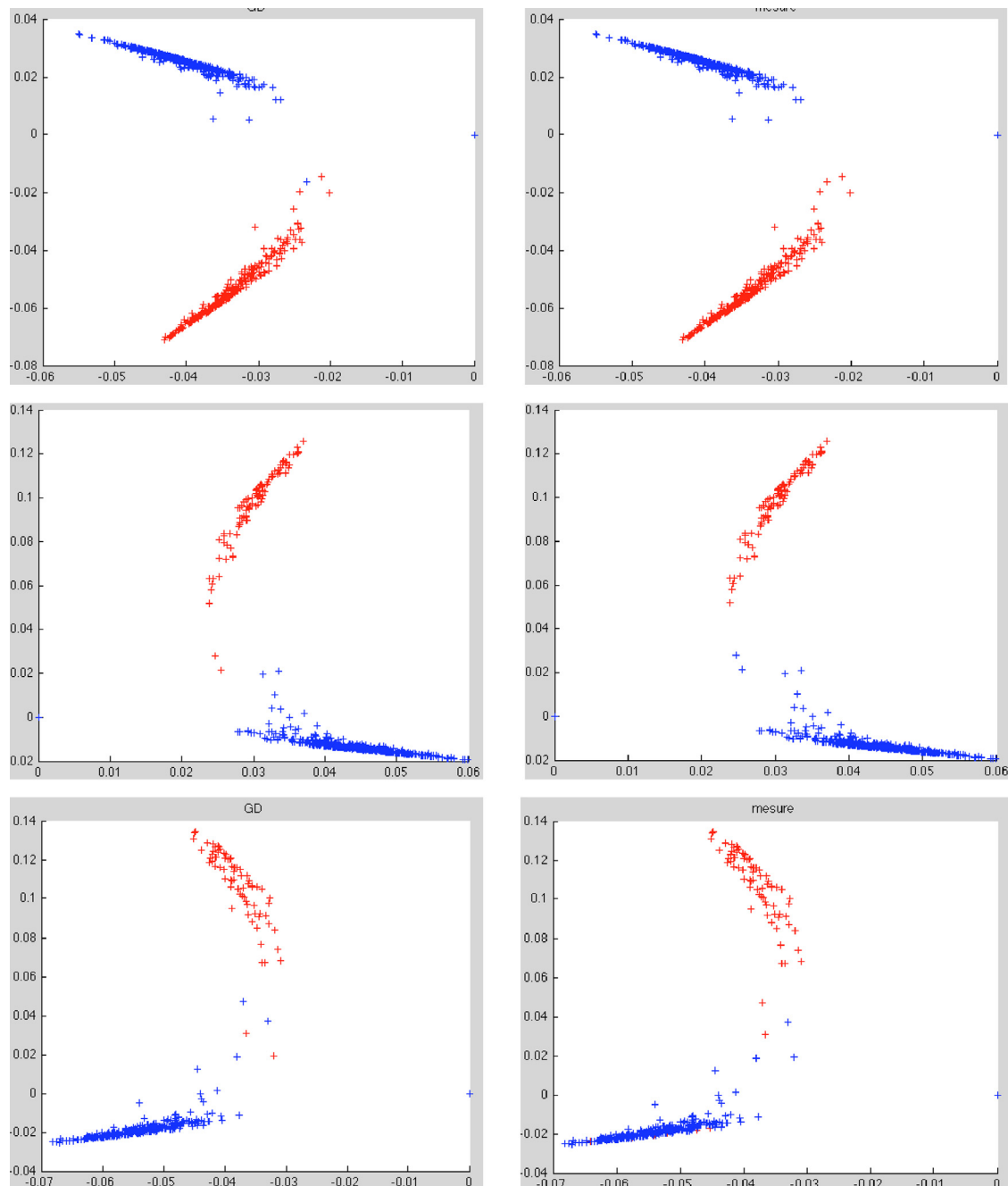


Fig. 8. Data plots following projection into the spectral map obtained by the two first eigenvectors and the merging application. Results are shown for case 1, case 2, and case 4. Left column is the ground truth, whereas the right column represents the outputs of the clustering algorithm.

For the last case, initially the algorithm classified the voxels into the two closest classes with signal behavior far from the reference artery signal; however, they were later merged into one homogeneous class. This finding may reflect the fact that the tissue in this zone presented a different response to the contrast agent than the artery and was thus considered as healthy.

A more precise analysis of our findings allowed for the following interpretations: in cases 1, 2, 4, and 5 the algorithm was able to effectively detect the tumors due to good tissue vascularization; however, results for the third case were not convincing. To understand the reasons for this behavior, we estimated the pharmacokinetic parameters using the Toft's model. The K_{trans} map (Fig. 10) confirmed the fact that the tissue examined for case 3 was poorly vascularized, likely representing a necrotic tumor.

5. Discussion and conclusion

Assuming that time-intensity curves are an indicator of tissue behavior, we proposed an original analysis method for DCE-MRI signals based on the grouping of voxels with similar behaviors. These behaviors can then be compared to a reference extracted from an artery. For this method, which is based on spectral clustering, the data are represented in graphical form with each vertex associated with a data sample and the weighted edges encoding the relationship between the underlying data. In contrast to commonly used techniques, such as K-means and mixture models, it is known that spectral clustering can deal with complex and unknown cluster shapes. In particular, the top eigenvectors of the graph Laplacian can unfold the data structure to form meaningful clusters.

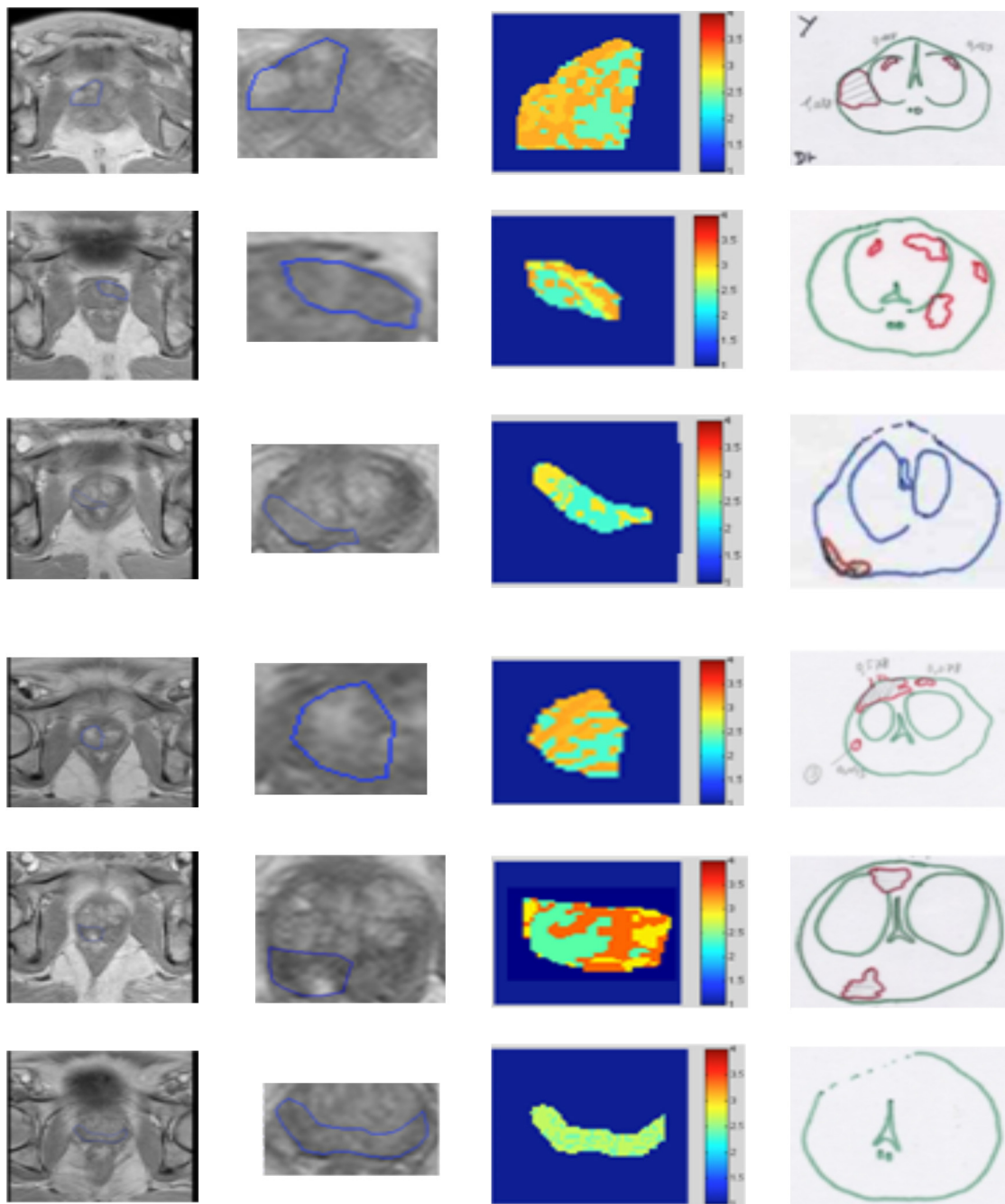


Fig. 9. Results obtained following application of the spectral clustering algorithm to clinical DCE-MRI of prostate. Five tissues with tumors in different localizations were examined. The last case was healthy tissue. From left to right: ROI of the images, zoom of the ROI, clustering results displayed as a distance map from the artery, and the ground truth (i.e., histopathology cards).

In comparison to methods that measure pharmacokinetic parameters or other data analysis techniques, our approach is non-parametric and fully automatic. Without making any assumptions regarding the models, our strategy exhibited results similar to those obtained by pharmacokinetic approaches. However, it is important to stress that our proposed method is not intended to replace pharmacokinetic techniques, but instead is meant to act a complementary analysis framework, which can ultimately help define cutoffs.

Another clustering-based method, which was described by Chen et al. [15], also represents a statistical data analysis method; however, it is parametric and assumes a Gaussian distribution of signal curves. We have validated our method using both synthetic and

clinical data. For the initial experiments on simulated cases, time concentrations and time-intensity curves with ground truths were constructed based on a previous method [15]. In order to make the simulations more realistic, they were combined with a 3D frame to obtain 4D images [29]. Indeed, the results of our experiments were very good, and the algorithm was able to detect lesions in all cases (Table 1). The data for the healthy case, in which no lesions were simulated, were also interesting. In fact, our algorithm highlighted the fact that the tissue was homogeneous following the analysis of cluster fusion and distance comparisons with the artery (Fig. 7).

For the second experiments, clinical data from routine prostate cancer imaging protocols were examined. Notably, histopathological data provided ground truths for the analysis, and our algorithm

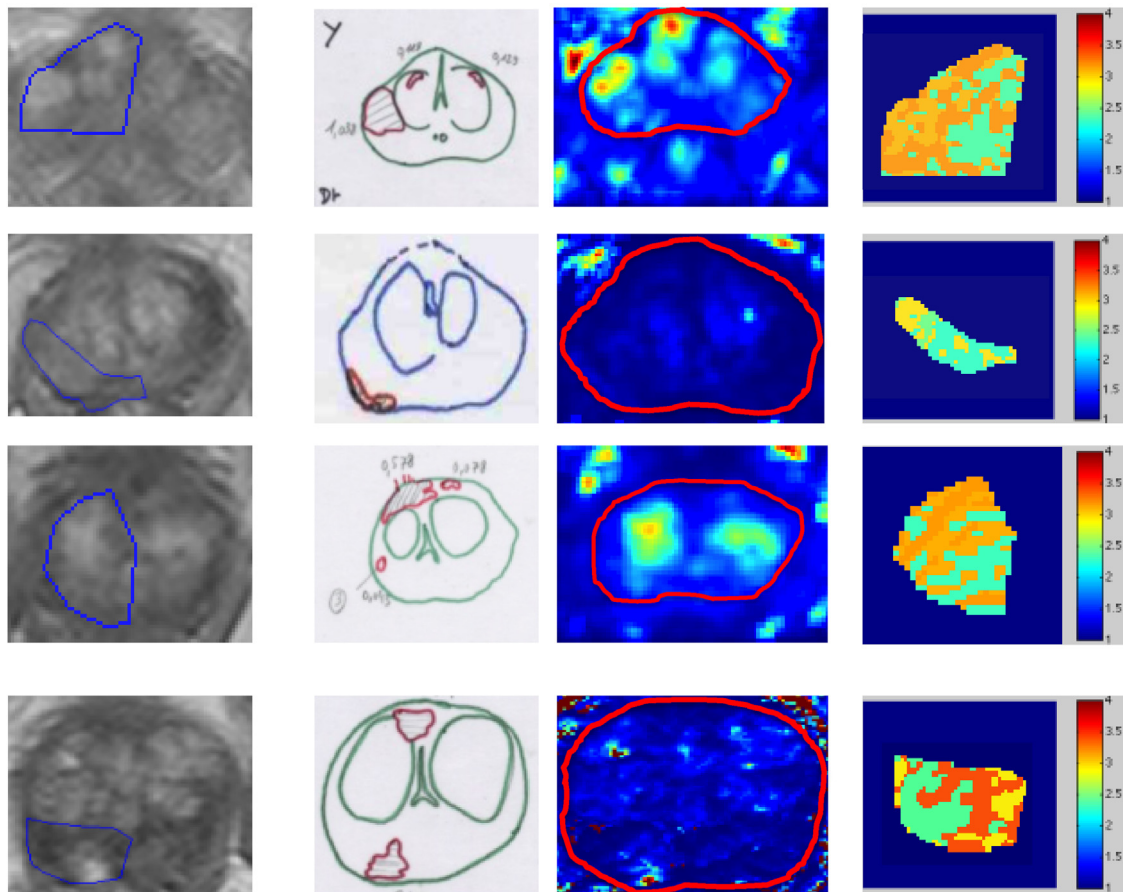


Fig. 10. Comparison of the results from the proposed method to K_{trans} maps (cases 1, 3, 4 and 5). From left to right: ROIs of the images, the ground truth, results of K_{trans} map, and clustering results displayed as a distance map from the artery.

proved to be efficient for assessing clinical cases (Figs. 9 and 10). However, these results must be related to DCE-MRI in order to establish the efficiency of localization. Indeed, it has been reported that for tumors with significant volumes (>0.5 mL) and Gleason grades (≥ 6), DCE-MRI shows sensitivity and specificity ranges of 46–96% and 74–96%, respectively [35].

Certainly, pharmacokinetic methods, such as Toft's model, cannot not be substituted by statistical techniques during DCE-MRI analysis. However, these methods can provide valuable information, which has been demonstrated in the present work as well as by others. Currently, we are investigating the optimal combination of these approaches within the same methodological framework, and our ultimate goal is to establish a standardized analysis and interpretation pathway that will yield excellent sensitivity and specificity.

References

- [1] Padhani AR. MRI for assessing antivasculature cancer treatments. *Br J Radiol* 2003;76(Spec No 1):S60–80.
- [2] Folkman J, Hanahan D. Switch to the angiogenic phenotype during tumorigenesis. *Princess Takamatsu Symp* 1991;22(339):347.
- [3] Izawa JI, Dinney CP. The role of angiogenesis in prostate and other urologic cancers: a review. *CMAJ* 2001;164(5):662–70.
- [4] Yancopoulos GD, Davis S, Gale NW, Rudge JS, Wiegand SJ, Holash J. Vascular-specific growth factors and blood vessel formation. *Nature* 2000;407(6801):242–8.
- [5] Buckley D, Parker RC, Logue G, Hutchinson JC. Prostate cancer: evaluation of vascular characteristics with dynamic contrast-enhanced T1-weighted MR imaging-initial experience. *Radiology* 2004;233:709–15.
- [6] Yankeelov TE, Gore JC. Dynamic contrast enhanced magnetic resonance imaging in oncology: theory, data acquisition analysis and examples. *Curr Med Imaging Rev* 2009;3(2):91–107.
- [7] Kuhl CK, Mielcareck P, Klaschik S, Leutner C, Wardelmann E, Gieseke J, et al. Dynamic breast MR imaging: are signal intensity time course data useful for differential diagnosis of enhancing lesions? *Radiology* 1999;211(1):101–10.
- [8] Puech P, Betrouni N, Makni N, Dewalle AS, Villers A, Lemaitre L. Computer assisted diagnosis of prostate cancer using DCE-MRI data: design, implementation and preliminary results. *Int J Comput Assist Radiol Surg* 2009;4(1):1–10.
- [9] Alonzi R, Taylor NJ, Stirling JJ, d'Arcy JA, Collins DJ, Saunders MI, et al. Reproducibility and correlation between quantitative and semiquantitative dynamic and intrinsic susceptibility-weighted MRI parameters in the benign and malignant human prostate. *J Magn Reson Imaging* 2010;32(1):155–64.
- [10] Parker GJ, Suckling J, Tanner SF, Padhani AR, Revell PB, Husband JE, et al. Probing tumor microvasculature by measurement, analysis and display of contrast agent uptake kinetics. *J Magn Reson Imaging* 1997;7(3):564–74.
- [11] Quantitative imaging biomarkers alliance. DCE MRI quantification profile; 2012. <http://rsna.org/QIBA.aspx>
- [12] Kershaw LE, Buckley DL. Precision in measurements of perfusion and microvascular permeability with T1-weighted dynamic contrast-enhanced MRI. *Magn Reson Med* 2006;56(5):986–92.
- [13] Wu XY, Liu GR. Application of independent component analysis to dynamic contrast-enhanced imaging for assessment of cerebral blood perfusion. *Med Image Anal* 2007;11:254–65.
- [14] Mehrabian H, Chopra R, Martel AL. Calculation of intravascular signal in dynamic contrast enhanced-MRI using adaptive complex independent component analysis. *IEEE Trans Med Imaging* 2013;32(4):699–710.
- [15] Chen Li, Choyke LP, Chan TH, Chi CY, Wang G, Wang Y. Tissue-specific compartmental analysis for dynamic contrast-enhanced MR imaging. *IEEE Trans Med Imaging* 2011;30(12):2042–58.
- [16] Agner SC, Xu J, Madabhushi A. Spectral embedding based active contour (SEAC) for lesion segmentation on breast dynamic contrast enhanced magnetic resonance imaging. *Med Phys* 2013;40(3):032305–32315.
- [17] Jia H, Ding S, Xu X, Nie R. The latest research progress on spectral clustering. *Neural Comput Appl* 2013. <http://dx.doi.org/10.1007/s00521-013-1439-2> [Damascus, Syria].
- [18] Ng AY, Jordan MI, Weiss Y. *Advances in Neural Information Processing Systems*, 14. MIT Press; 2001. p. 849–56.
- [19] Shi J, Malik J. Normalized cuts and image segmentation. *IEEE Trans Pattern Anal Mach Intell* 2000;22:888–905.

- [20] von Luxburg U. A tutorial on spectral clustering. *Stat Comput* 2007;17(4):395–416.
- [21] Hamad D, Biela P. Introduction to spectral clustering. In: 3rd international conference on information and communication technologies: from theory to application. 2008.
- [22] Zelnik-Manor L, Perona P. Self-tuning spectral clustering, part of advances. In: Neural information processing systems 17. 2004.
- [23] White S, Smyth P. A spectral clustering approach to finding communities in graph. In: Proceedings of SDM. 2005.
- [24] Newman MEJ, Girvan M. Finding and evaluating community structure in networks. *Phys Rev* 2004;69(13):0261.
- [25] Network community discovery: solving modularity clustering via normalized cut; 2010.
- [26] Cinotti L, Bazin JP, Dipaola R, Susskind H, Brill AB. Processing of Xe-127 regional pulmonary ventilation by factor analysis and compartmental modeling. *IEEE TMI* 1991;10(3):437–44.
- [27] Kruggel F, von Cramon DY, Descombes X. Comparison of filtering methods for fMRI datasets. *Neuroimage* 1999;10(5):530–43.
- [28] Chen J, Yao J, Thomasson D. Automatic determination of arterial input function for dynamic. *Med Image Comput Comput Assist Interv* 2008;11(Pt 1):594–601.
- [29] Betrouni N, Iancu A, Puech P, Mordon S, Makni N. ProstAtlas: a digital morphologic atlas of the prostate. *Eur J Radiol* 2012;81:1969–75.
- [30] Weinmann HJ, Laniado M, Mutzel W. Pharmacokinetics of GdDTPA/dimeglumine after intravenous injection into healthy volunteers. *Physiol Chem Phys Med NMR* 1984;16(2):167–72.
- [31] Kershaw LE, Hutchinson CE, Buckley DL. Benign prostatic hyperplasia: evaluation of T1, T2, and microvascular characteristics with T1-weighted dynamic contrast-enhanced MRI. *J Magn Reson Imaging* 2009;29(3):641–8.
- [32] Aerts HJ, van Riel NA, Backes WH. System identification theory in pharmacokinetic modeling of dynamic contrast-enhanced MRI: influence of contrast injection. *Magn Reson Med* 2008;59(5):1111–9.
- [33] McNeal JE, Haillot O. Patterns of spread of adenocarcinoma in the prostate as related to cancer volume. *Prostate* 2001;49:48–57.
- [34] Haffner J, Potiron E, Bouyé S, Puech P, Leroy X, Lemaitre L, et al. Peripheral zone prostate cancers: location and intraprostatic patterns of spread at histology. *Prostate* 2009;69(3):276–82.
- [35] Verma S, Turkbey B, Muradyan N, Rajesh A, Cornud F, Haider MA, et al. Overview of dynamic contrast-enhanced MRI in prostate cancer diagnosis and management. *AJR Am J Roentgenol* 2012;198:1277–88.